Applied Catalysis B: Environmental 338 (2023) 123023

Contents lists available at ScienceDirect

Applied Catalysis B: Environmental

journal homepage: www.elsevier.com/locate/apcatb

Intramolecular built-in electric field enhanced polymerized nitrogen-carbon homojunction π*-electron delocalization enrichment promotes photocatalytic uranium (VI) reduction

Zhangmeng Liu [a], Shuaiqi Yao [b], Anran Zhang [b], Yayao Li [b], Yunzhi Fu [b,*], Qixin Zhou [c,*]

[a] School of Materials Science and Engineering, Hainan University, Haikou 570228, PR China
[b] School of Science, Hainan University, Haikou 570228, PR China
[c] Department of Chemistry, Tsinghua University, Beijing 215123, PR China

ARTICLE INFO

Keywords:
Conjugated molecule
Polymerized nitrogen-carbon
Homojunction
Built-in electric field
U(VI) reduction

ABSTRACT

The donor-acceptor (D-A) structure in conjugated systems enhances photogenerated carrier separation efficiency due to π * electron delocalization resulting from π-π interactions. This study reports a conjugated molecular carbon-nitrogen homojunction (CNH) with inherent π * electron transitions, which intrinsically enriches electron-hole pairs in the energy band region via its built-in electric field. CNH's intermolecular π-π stacking promotes efficient U(VI) reduction by boosting carrier generation and separation. Compared to CNNH, formed by temperature-controlled thermal polymerization of melamine and urea, the introduction of -NH_2 disrupts the 3-s-heptazin ring in CNH's conjugated system. Heptazine integrity directly affects π-π * electron enhancement and transition, leading to a significant decrease in U(VI) reduction efficiency. Specifically, CNH exhibits optimal efficiency, reducing U(VI) by 99.6% within 60 min. This work emphasizes the significance of strong built-in electric fields generated through intramolecular π-π stacking, stimulating π-π * transitions, and enriching photogenerated π * electrons in carbon-nitrogen polymers, ultimately improving U(VI) photoreduction.

1. Introduction

Due to its unparalleled advantages, nuclear energy has experienced rapid growth, leading to a significant increase in wastewater containing radionuclide uranium. Addressing these environmental pollutants and enriching uranium nuclides are essential in the era of spent fuel [1–3]. Photocatalytic reactions [4–6], which utilize abundant solar energy and offer eco-friendly advantages [7–9], are employed in various applications such as heavy metal pollution ion removal [10–12], and degradation of organic compounds in wastewater and air pollutants [13–16]. These applications and developments are strongly dependent on the carrier separation efficiency of photocatalysts, despite the majority of research focusing on enhancing photocatalytic efficiency through heterostructure and defect engineering [17–21], it is crucial to note the distinct solubility of oxidized uranium in different valence states. The application of photocatalytic technology to reduce soluble U (VI) in the environment to insoluble and relatively fixed U (IV) species provides a feasible solution, thus achieving safer treatment of uranium-containing wastewater. Therefore, a deeper understanding of photocatalytic efficiency is needed. There is an urgent need to enhance the carrier transfer mechanism in the results while concurrently improving carrier generation and separation efficiency in the photocatalytic reduction of uranium U(VI) [22–26].

The s-heptazine and triazine molecules, characterized by their conjugated π systems with high electron affinity, exhibit unique optical and electronic behaviors [27]. Recent developments in carbon nitride polymers (PCN), covalent triazine frameworks (CTFs), and poly-triazine imides (PTIs) indicate their potential as organic photocatalysts for total water splitting, sharing structural features with N-containing aromatic heterocycles [28]. Some cutting-edge studies have shown that the N atoms of aromatic heterocycles usually have an essential impact on the catalyst activity through electronic and steric hindrance changes, which provides a direction for regulating the structure of the oxazine ring at the molecular level to design efficient and active catalysts [29]. In addition, π-conjugated structure with discontinuous π-electron delocalization throughout the framework [30–32], these efficient charge and energy transfers have enabled the catalyst mentioned above materials to be used in many fields, such as photovoltaics [33], sensors [34] and

* Corresponding authors.
E-mail addresses: yzhfu@hainanu.edu.cn (Y. Fu), zqx20@mails.tsinghua.edu.cn (Q. Zhou).

https://doi.org/10.1016/j.apcatb.2023.123023
Received 2 April 2023; Received in revised form 2 June 2023; Accepted 19 June 2023
Available online 20 June 2023
0926-3373/© 2023 Elsevier B.V. All rights reserved.

heterogeneous Catalysis [35–37]. However, the synthesis of most CTFs and PTIs with triazine structures involves toxic reagents and complex processes. Thus, there is a strong demand for rapid, environmentally friendly, and cost-effective approaches to obtain triazine molecules with efficient optical and electronic properties.

Polymeric carbon nitride (PCN) is widely recognized for its simple synthetic raw materials [38–40]. Consequently, its various physical and chemical properties can be regulated by controlling the chemical composition of raw materials and altering synthesis steps, impacting the material's morphology, crystallinity, photogenerated carrier separation efficiency, and exciton migration behavior [41–43]. Specifically, unique 3-s-triazine ring structure makes the C and N atoms in the structure hybridized by sp2 to form a highly delocalized π-conjugated system [44–46]. In addition, at the molecular level, more stable triplet states of aggregates can be formed through intramolecular π - π stacking, which excites the π - π * transition characteristics of conjugated structures, which can effectively enhance the efficiency of photogenerated carrier separation, the movement range of π * electrons are no longer limited to two carbon atoms, and the transition is transferred through the conjugated system of PCN. The typical ones are π→π * electronic transition and n→π * transition [47–49]. Different types of electronic transitions help to generate carriers during the transition process. The carrier density and separation efficiency determine the efficiency of photocatalytic reduction of uranium U(VI).

On the basis of the above research, we obtained a nitrogen-carbon homojunction (CNH) synthesized by a specific ratio of melamine and urea by adjusting the composition of the raw materials for the synthesis of PCN [50]. The ultra-thin nitrogen-carbon homojunction with an intramolecular donor-acceptor (D-A) structure generated a strong interfacial built-in electric field (IEF) due to C-N single bond induction and -C═N bond-mediated π * electron transition. The photogenerated electrons and holes of the conjugated molecule CNH are selectively enriched in its valence band and conduction band regions, respectively. With adding sacrificial hole agent (methanol), the reduction reaction of U(VI) is facilitated by the π * electron transition. To demonstrate the electronic transition and enrichment of CNH formed under a specific ratio due to its complete intramolecular π-π stacking conjugated system, we also synthesized a CNNH rich in amino (-NH_2) using raw materials containing melamine, urea, and hydroxylamine hydrochloride. The U (VI) reduction experiment showed that the introduction of -NH_2 disrupted electron transfer in the CNH conjugated system, directly impacting the generation enhancement and transition of π * electrons, leading to a significant decrease in U(VI) reduction efficiency. In conclusion, CNH exhibited the highest efficiency in reducing U(VI), effectively reducing 99.6% of 50 ppm U(VI) within 60 min, with excellent stability and cycle performance.

2. Experimental section

2.1. Preparation of MCN (Ox-CN)、UCN (Re-CN)、CNH、CNNH

Specifically, we carried out a step-by-step coating process on the raw materials for the synthesis of CNH. First, urea (7.25 g) and melamine (2.75 g) are dissolved separately in boiling water during sample preparation and sprayed in sequence. Then the melamine was sprayed into the preheated inside crucible (120 °C), put the crucible in a drying oven (120 °C), and waited for the water to evaporate completely. At this time, the melamine has spread evenly on the inner wall of the crucible, and then spray urea on its surface and wait for the crucible to dry again. After the water is completely evaporated, a phase-separated precursor coating structure is obtained. At this time, the crucible is placed in the muffle furnace, and the heating rate is set to 10 °C min^{-1}. The heating rate is set at 550 °C for 2 h, then slowly cool to room temperature at a cooling rate of 1 ℃ min^{-1}. The obtained CNH solids were collected and directly used for photocatalytic experiments. Similarly, by replacing the precursors in the above method with 10 g of urea or melamine, UCN (marked as Re-CN) and MCN (marked as Ox-CN) can be obtained; the precursors are replaced with 6.25 g of urea, 2.75 g melamine, and 1 g hydroxylamine hydrochloride were roasted in the same steps to obtain CNNH.

2.2. Photocatalytic experiments

The concentration of U (VI) used in this photocatalytic reduction of uranium experiment is 50 ppm, the theoretical maximum limit of nuclear wastewater, and the solid-liquid ratio is 0.1 g·L^{-1}. Photocatalysis experiments were carried out by circulating condensed water to ensure the reaction temperature was close to room temperature (T = 298 K). Briefly, dissolve 5 mg of photocatalyst in 50 mL of $UO_2(NO_3)_2$·6 H_2O solution and ultrasonically disperse evenly, then transfer the suspension to a 50 mL jacketed quartz open beaker and stir for 60 min in the dark to ensure that the adsorption kinetic equilibrium is reached. Then the reactor was placed under a 300 W Xenon light source, and 2 mL of anhydrous methanol was added as a hole sacrificial agent before starting the reaction. During the reaction, 1 mL of the suspension was taken every 5 min. The sample was filtered through a 0.22 μm membrane to filter the supernatant. The removal efficiency of U (VI) in the supernatant was measured by arsenazo III spectrophotometry. Photoreduction experiments were carried out in three groups of parallel experiments at the same time, and the average value was used as the source data. The removal rate is calculated according to the following formula: U (VI) removal rate (%) = (C_0 - C) / C_0 × 100%.

In the recovery experiment, the suspension was centrifuged and the supernatant was removed after irradiation for 2 h. The photocatalyst was regenerated by immersing the solid phase in 1 M NH_4HCO_3 aqueous solution and stirring for 12 h to release uranium. After washing with water, the collected samples are used for the next cycle. In order to study the effect of different strong interference ions on the photoreduction of U (VI). In the interference experiment, NaCl, KCl, $CaCl_2$, $FeCl_3$, Na_2CO_3 and $NaHCO_3$ of 50 ppm were mixed with U (VI) of 50 ppm respectively. In addition, photocatalytic experiments about different pH values were also carried out. Other more detailed lab details and DFT calculation details can be found in the Support Information.

3. Results and discussion

As shown in the preparation process of Fig. 1(a), expressly, by dissolving and sequentially spraying the precursors (urea, melamine) for the preparation of synthetic CNH, a phase-separated precursor coating membrane structure was obtained in a smooth crucible lining; as we recognize, urea will generate melamine intermediates through a series of thermal decomposition polymerization reactions during the thermal polymerization heating process, the intermediate product melamine will be mixed with the melamine precursor of the lining film under the protection of the ammonia atmosphere environment at 500 °C, and then thermal polymerization occurs at 550 °C to form solid phase Ox-CN, which also becomes a bridge to build CNH. At the same time, urea undergoes thermal decomposition at 550 °C to form solid phase Re-CN and is finally combined to control the cooling rate during thermal polymerization [51]. The heptazine ring structures in the Ox-CN and Re-CN structures are connected by hydrogen bonds and form π-π stacking through van der Waals forces to obtain nitrogen-carbon homojunction nanosheets (CNH); for comparison, melamine, urea, and hydroxylamine hydrochloride as raw materials through thermal polymerization process obtained monomer MCN nanosheet structure, UCN nanosheet structure, and CNNH nanosheet structure.

Fig. 1(b)~(e) shows the SEM images of PCNs synthesized by thermal condensation of different precursors, in which a more obvious agglomeration phenomenon can be observed in Fig. 1(d)(e). In sharp contrast, due to the slight difference in the precursor composition (urea, wt%) during thermal polymerization, CNH and UCN both exhibit fluffy nanofragmented structures, and the agglomeration phenomenon is well suppressed (Fig. 1(b)(c) represented). Pores and fragmented forms are

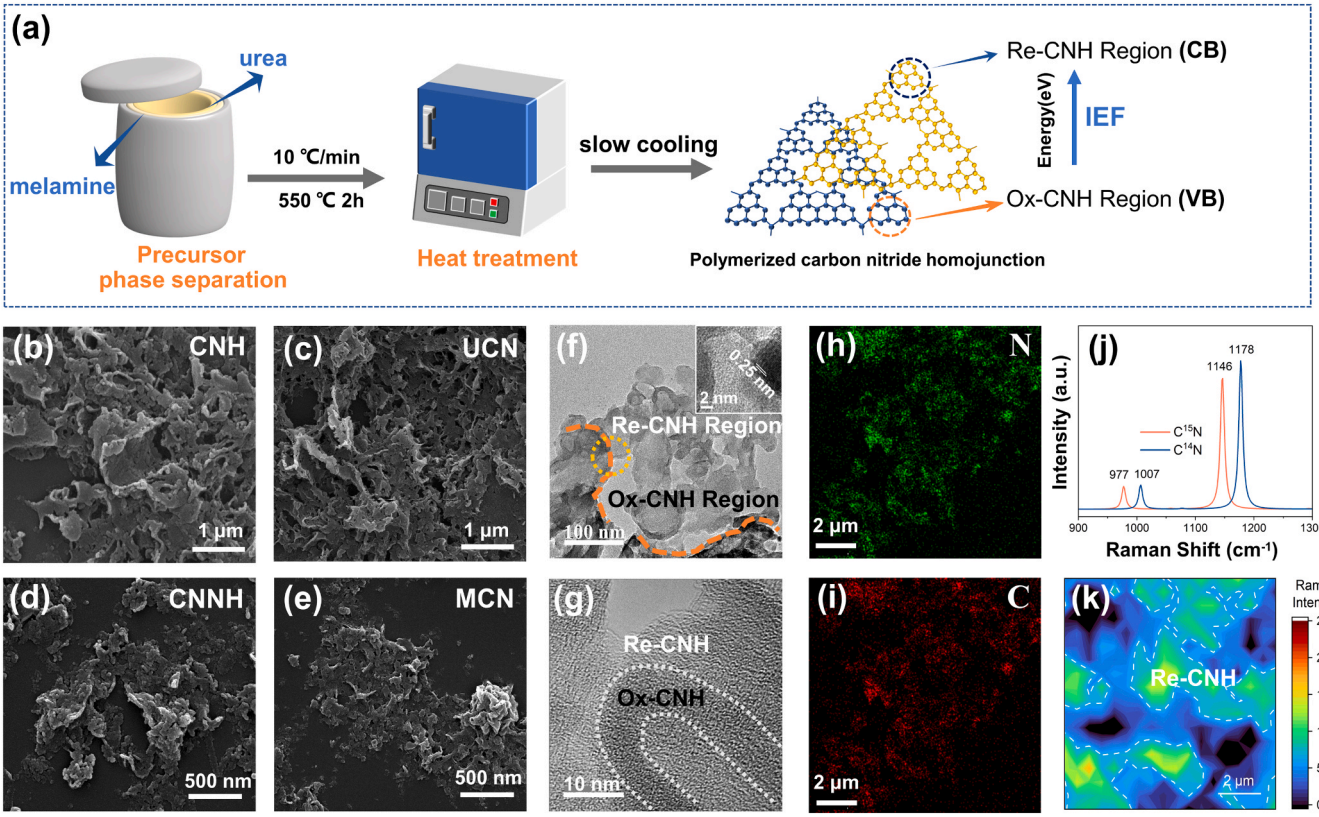

Fig. 1. (a) Schematic diagram of CNH preparation process, (b) - (e) SEM images of CNH, UCN, CNNH, and MCN, (f) HR-TEM images of CNH (the illustration is a locally enlarged lattice image), (g) HR-TEM images of CNH, (h) - (i) EDS mapping of CNH, (j) (k) Raman Intensity of CNH.

conducive to the separation and partitioning of carriers in the highly delocalized π-conjugated system of CNH excited by light. Specific surface area investigation can also prove this point. (Fig. S6) At the same time, more light reflection and scattering phenomena will be added, and the absorption of visible light by CNH will be improved, which is conducive to generating more electrons and hole pairs, which are beneficial to promote the improvement of photocatalytic activity. The characterization results of TEM (Fig. 1(f)(g)) can show the phase separation region of CNH more clearly, in which the Re-CN region formed by the higher mass fraction of urea in the precursor composition is displayed as a light-colored flat transparent disordered amorphous structure, while the Ox-CN region formed by the thermal polymerization of another component in the precursor, melamine, has better crystallinity and is shown as a dark region. Fig. S1 provides more detailed HR-TEM

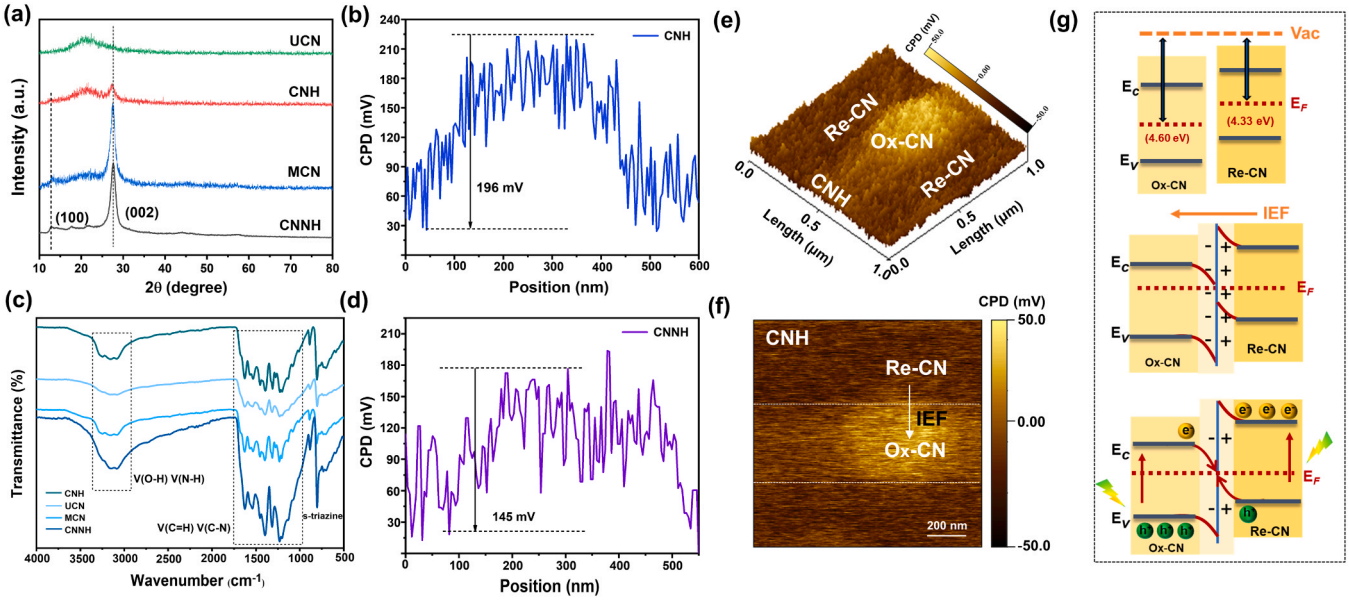

Fig. 2. (a) Powder X-ray diffraction (PXRD) patterns of each catalyst, (c) Fourier transform infrared (FT-IR) spectra of each catalyst, (b) (d) Contact potential difference (CPD) between CNH and CNNH, (e) (f) KPFM image of CNH, (g) Energy band shift and interface charge characteristics of CNH.

images of each catalyst. The interface of different conjugated domains in CNH can visually observe through high-resolution TEM (HR-TEM). A lattice stripe spacing of 0.25 nm is displayed in the Ox-CN region, which can correspond to a planar heptazine ring structure [46]. However, the HR-TEM of Re-CN shows a more disordered amorphous structure, and no prominent lattice fringes can be observed. Through single-point energy dispersive spectrometer (EDS) analysis (Fig. S2), there is a significant difference in element ratio between CNH and CNNH. The decrease of the C/N element ratio in CNNH proves the successful introduction of $-NH_2$. In addition, we also used the 15 N labeling of the precursor urea molecule to test the Raman peak of the thermal polymerization product. It can be seen from the Fig. 1(j) (k), using the DFT theoretical spectrum B3LYP 6–311 +G*em = gd3bj for dispersion correction, the frequency and Raman intensity were optimized and measured at this level, the obvious partition structure of Re-CN can also be found.

Powder X-ray diffraction (PXRD) used to confirm the crystal structure of CNH. We tested the crystal structure properties of all samples (Fig. 2(a)). It can be observed that the four samples have two independent diffraction peaks at ~27.5° and ~13.1°, the (002) crystal plane of the conjugated aromatic system and the superimposed planar structure (100) crystal plane, respectively assigned to the layered oxazine ring structure, indicate the conjugated structure of CNH layered stacking [43]. Among them, it can be seen that the (002) diffraction peak of MCN is the narrowest and sharpest, indicating that this material has a high degree of crystallinity. This can provide convenience for distinguishing Ox-CN and Re-CN from CNH. Compared with other monomeric PCN materials, CNH homojunction materials have significantly broader XRD diffraction peaks and weaker intensity, which can be attributed to the shortening of the periodic arrangement distance between CNH framework layers due to the more minor size effect of CNH nanomaterials. In order to clarify the molecular structure of CNH homojunction and CNNH and two single-phase CN materials, all samples were tested and compared by FT-IR, as shown in Fig. 2(c). It can be seen from the characterization results that the four monomer materials have similar FT-IR spectra, which proves that they all have the basic structure of CN [48]. The breathing vibration of the 3-s-triazine ring structure can correspond to the peak at the wavenumber of 809 cm^{-1}; the vibration of the aromatic ring structure can correspond to the peak at the wavenumber of 810 ~ 1700 cm^{-1}; the vibration of the carbon-nitrogen single bond and double bond respectively correspond to 1320 cm^{-1} and 1640 cm^{-1}; the N-H of the imino group in the structure and the O-H vibration absorption peak of the adsorbed water molecule can be speculated to be the wave number of 3000 ~ 3400 cm^{-1} [38], which proves that the highly conjugated π-π stacking structure of CNH provides conditions for photo-excited π * electron generation and delocalization.

Then, the distribution of IEF in CNH was investigated using Kelvin

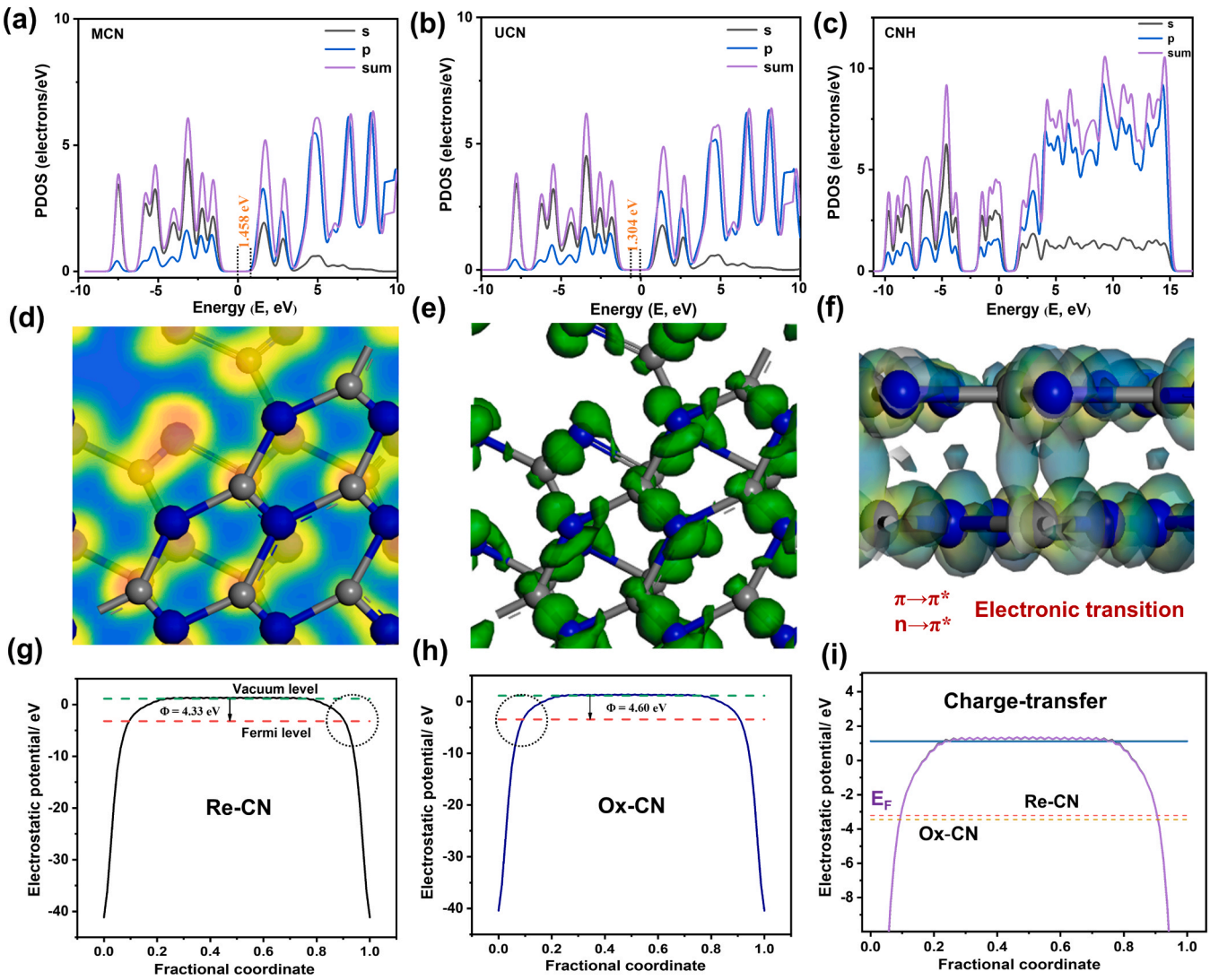

Fig. 3. The energy band structure and corresponding density of states of (a) MCN, (b) UCN, and (c) CNH; (d) (e)The charge density difference between Re-CN and Ox-CN within CNH; (f) Charge transfer channels in CNH conjugated molecules; (g) - (i) Difference of Electrostatic potential for Re-CN and Ox-CN.

probe force microscopy (KPFM). It is well known that KPFM images provide the contact potential difference (CPD) between the tip and the sample, and the surface potential of semiconductors is characterized due to differences in their structures [52–54]. As shown in Fig. 2(e) (f), the KPFM image of CNH clearly shows the characteristic regions of Re-CN and Ox-CN that are separated in space. At the same time, Fig. 2(b) (d) shows the CPD of CNH and CNNH. It can be seen that the CNH appears to have a noticeable area separation contact potential difference (Fig. 2(f)), and the contact potential difference of 196 mV can be inferred as the Re-CN edge with the main body, the contact potential difference of 103 mV can be assumed as the contact potential difference between the Ox-CN edge between CNH with Re-CN, which demonstrated CNH is composed of partitions Re-CN and Ox-CN by the plateau appearing in Fig. 2(b). For comparison, CNNH only showed a contact potential difference of 145 mV (Fig. 2(d)). As we know, the CPD difference between the two regions can reflect the intensity of IEF in the substance, and the test results of KPFM show a larger IEF in CNH [53].

Next, we explored the possible transfer direction of photogenerated carriers at the CNH interface [43]. Fig. 3(g)(h) shows the work functions of Re-CN and Ox-CN obtained by simulation calculations based on density functional theory (DFT), which are almost identical to the CPD test results, which fully demonstrates the accuracy of our simulated presentation of differential charge density and carrier transfer results in CNH. Fig. 3(a)~(c) shows the PDOS of each PCN respectively. It can be seen that the PCN energy band is mainly composed of 1 s, and 2p orbitals, which also corresponds to the triazine structure in PCN. The results in Fig. 3(c) show that the carrier density in the conduction band (CB) and valence band (VB) energy of CNH is significantly enhanced, especially in the conduction band bottom (CBM) region of CNH, the electron density is increased dramatically, resulting in a more vital reducing ability of CNH.

In order to explore the specific reasons for the increase in carrier density, Fig. 3(d) (e) (f) further visually present the CNH charge density and charge transfer channel. Fig. 3(d)(e) simulates the plan view of the local charge density distribution of the CNH structure formed by the layered stacking of Re-CN (dark structure) and Ox-CN (Light-colored structure) conjugated aromatic structures. It can be seen that the charge density is higher around the atoms that form π * bonds in the aromatic ring. Combining with Fig. 3(f), it can be seen more clearly that a charge transfer channel appears between Re-CN and Ox-CN only through the complete conjugated structure, which can be attributed to the π - π * electron transitions in the aromatic ring structure.

The formation of IEF between CNH and the possible charge transfer mechanism between firmly contacting interfaces are determined by calculating the electrostatic potential of the material surface and obtaining the work functions of Re-CN and Ox-CN in Fig. 3(g)(h), which is an important physical parameter for free electron transfer and band alignment in homojunction. The changing trend of the Fermi level caused by the difference in the work function of the two components (Fig. 3(i)) can be interpreted by Fig. 2(g). As shown in Fig. 2(g), when Re-CN with high work function and Ox-CN with low work function are in contact, since the Fermi level needs to be balanced, electrons will pass through the tight interface of CNH homojunction from Re-CN migrates to Ox-CN, while holes migrate from Ox-CN to Re-CN [50,55]. At this time, a built-in electric field (IEF) will be generated between the two conjugated components, pointing from Re-CN to Ox-CN, thereby preventing the recombination of electrons and holes, and achieving the effect of carrier partition aggregation. Driven by IEF, the electrons on the CB of Re-CN gather to increase its potential energy, and the energy band bends upward. On the contrary, the potential energy of the CB on Ox-CN decreases and the energy band bends downward. At this time, the photogenerated electrons at the CB of Ox-CN will recombine with the holes at the VB of Re-CN through the contact interface [55], leaving the photogenerated holes to accumulate at the VB of Ox-CN and leaving photogenerated π * electrons gathered in the CB of Re-CN.

The chemical state of the elements in each catalyst was quantitatively determined by X-ray energy spectroscopy (XPS). Fig. 4(a)(b) shows each sample's XPS core level spectra of C 1 s and N 1 s. In the C 1 s spectrum, the peak at 284.8 eV for all samples corresponds to the impurity C element, which is used to calibrate the position of the energy spectrum. The peak at 288.1 eV corresponds to N-C═N in the heptazine structure, and the position of the peak in MCN is shifted to the high-energy region by 0.10 eV, which may be due to the higher crystallinity of MCN. The peak at 286.0 eV corresponding to the C═N structure also proves that high crystallinity leads to more C═N bonds in the MCN structure [44,45,51], which is consistent with the XRD characterization results. In the nuclear spectrum of N 1 s, the peak at 398.5 eV corresponds to C-N = C in the heptazine structure, 399.4 eV corresponds to the N-$(C)_3$ structure and 400.8 eV corresponds to the N-H structure. In particular, the peaks corresponding to the N-$(C)_3$ structure and N-H structure in CNNH are shifted to the high energy region by 0.19 eV and 0.18 eV [25], which can be attributed to the introduction of a large amount of -NH_2. All in all, the XPS results demonstrate that the existence and stacking of aromatic structures in the PCN structure will create conditions for the delocalization of π * electrons.

In order to investigate the energy band structure of the synthesized PCN photocatalyst, UV–visible diffuse reflectance spectroscopy (UV vis-DRS), and X-ray photoelectron valence band spectroscopy (VB XPS) were carried out. As shown in Fig. 4(d)(e), the absorption of CNH in the visible region increases obviously after recombination, and the optical absorption range of CNH extends from 400 nm to 600 nm, which can be attributed to the expansion of n→π * electron transition from π→π * electron transition in PCN conjugated structure. The band gaps of four kinds of PCN catalysts can be estimated from the tangent intercept by the Tauc plot method [1,56], which are CNNH (2.50 eV), CNH (2.57 eV), UCN (2.63 eV) and MCN (2.52 eV) from small to large. Generally speaking, the valence band and conduction band potential of typical PCNs can be calculated by the following empirical formula: $E_{CB}=E_{VB} - E_g$. The valence band edge positions of catalysts measured by VB XPS are CNNH (2.10 eV), CNH (2.05 eV), MCN (1.70 eV), and UCN (2.0 eV), respectively. Combined with UPS measured the position of the top of the valence band and the work function obtained through conversion (Fig. S8), we can get the CB positions are CNH (- 1.24 eV), MCN (- 1.54 eV), and UCN (- 1.35 eV), respectively. It is more negative than UO_2^{2+}/U^{4+} (0.267 eV) and UO_2^{2+}/UO_2 (0.411 eV), so it is feasible to remove/recover uranium by CNH photocatalysis.

Moreover, the apparent IEF as the driving force for interfacial charge transfer, we quantified the effective charge transfer efficiency of the Re-CN/Ox-CN interface by a model measurement developed by Kanata et al. [57–59]. We carefully calculated their charge density by transient photocurrent density measurement and surface photovoltage spectroscopy (SPV). Le Formal and Gratzel et al. reported that by integrating the measured transient photocurrent density minus the steady-state value of photocurrent relative to time [60–62], this value is proportional to the number of positive charges accumulated on the surface. The surface charge density of MCN, UCN and CNH is shown in Fig. 5(a); the surface photovoltage is obtained by measuring their surface photovoltage spectra (Fig. 5(b)). It can be found that the IEF of CNH is 16.5 times higher than that of MCN, which can significantly accelerate the interfacial charge separation. At the same time, we proposed the charge transfer pathway for the CNH structure (Fig. 4(c)). As shown in the figure, under light irradiation, due to the specific charge transfer channels at the interface of Re-CN and Ox-CN, high-energy electrons are enriched on the CB of Re-CN, and high-energy holes are accumulated on the VB of Ox-CN, thereby respectively driving the redox reaction. Benefiting from the larger IEF of CNH, the charge separation efficiency in CNH is quantified by transient photocurrent experiments, as shown in Fig. 5(d)~(f). CNH showed the highest charge separation efficiency of 87.3% [63–65]. Therefore, we can look forward to its efficient photocatalytic performance.

In the experiment of photocatalytic removal of U(VI), firstly, the reduction efficiency of UO_2^{2+} of each catalyst in a pure water system was

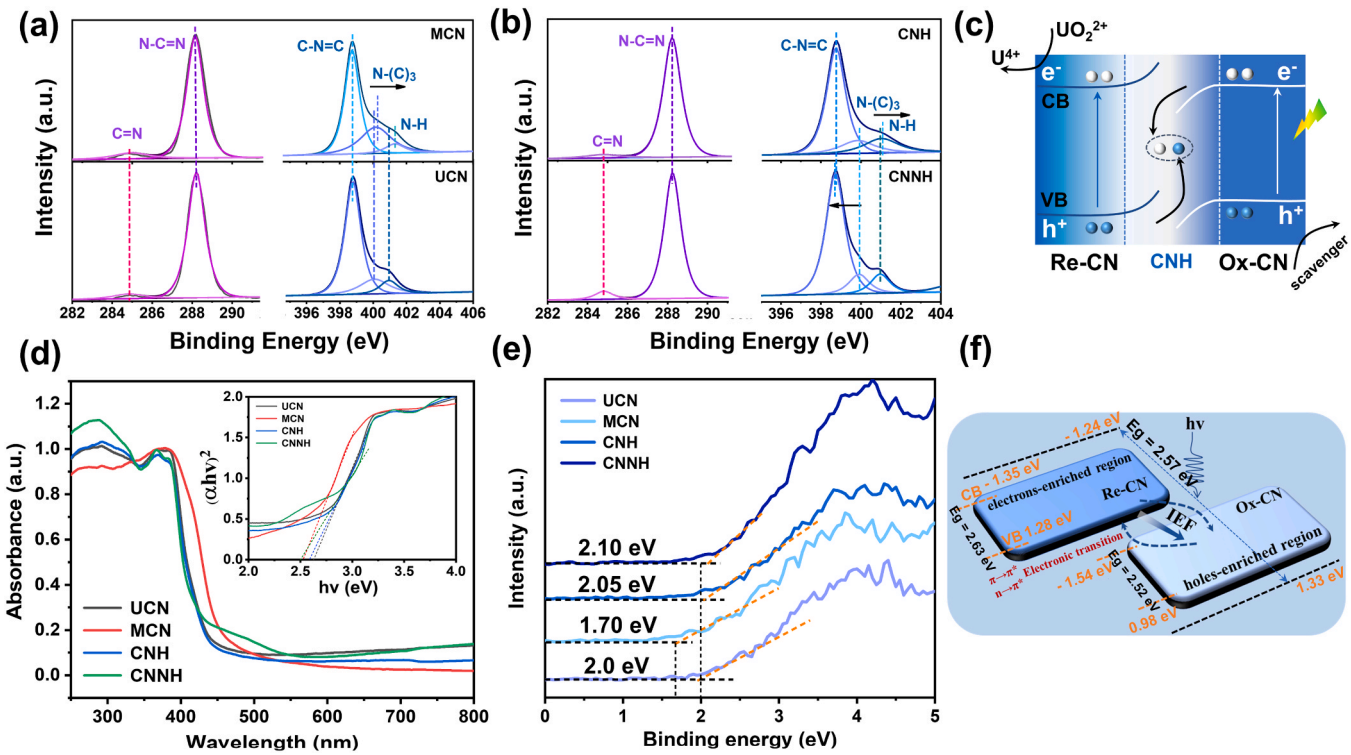

Fig. 4. . (a) (b) High-resolution XPS spectrum of the catalyst (C 1 s, N 1 s); (c) Energy band structure diagram of CNH; Tauc plot method for fitting curves of (d) UV–visible diffuse reflectance and semiconductor band gap for catalysts; (e) X-ray photoelectron valence band (VB-XPS); (f) Schematic of the coordinated IEF drives charge-transfer route in the CNH.

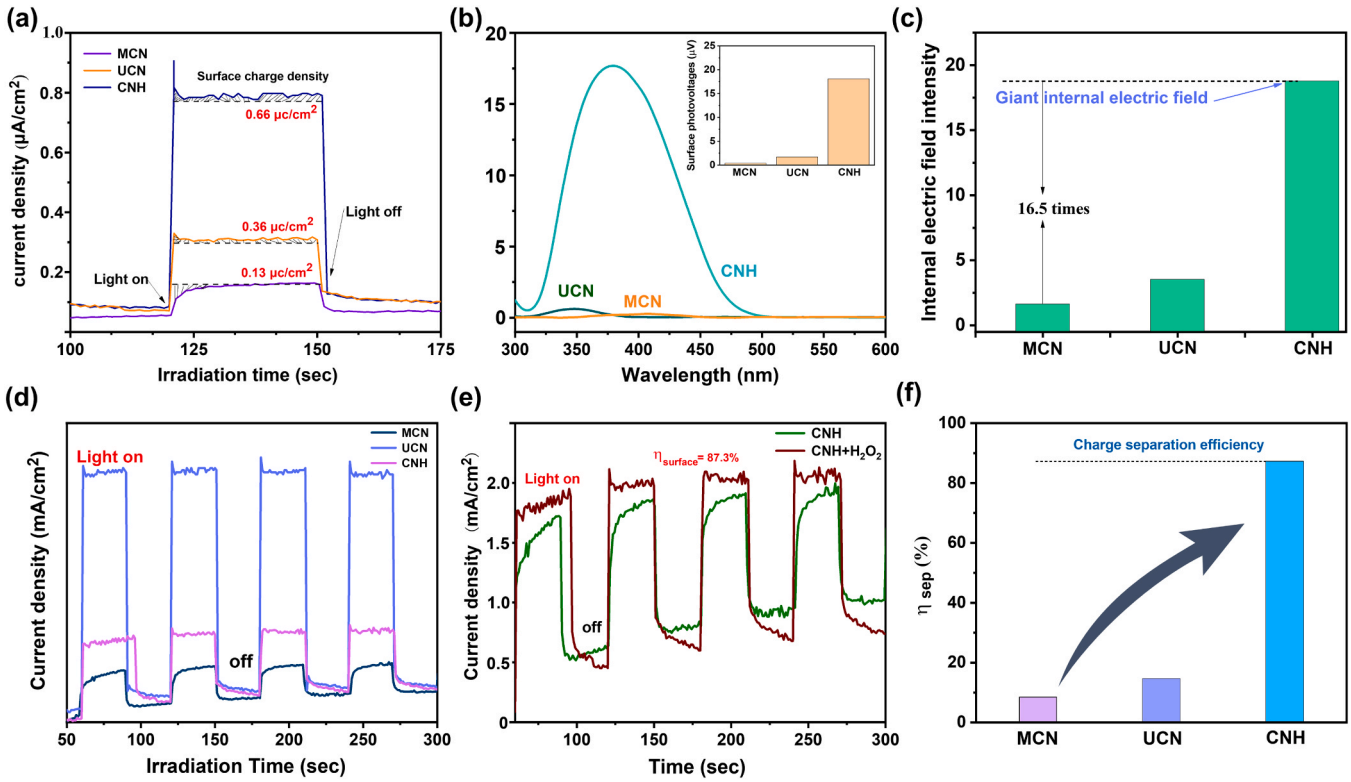

Fig. 5. (a) The surface charge density; (b) SPV spectrum and surface photovoltage intensity; (c) The internal electric field intensity of MCN, UCN, and CNH (assuming the intensity of MCN to be "1"); (d) Samples of transient photocurrent response; (e) The transient photocurrent density with and without adding H_2O_2 for CNH; (f) The comparison of charge separation efficiency of catalysts.

tested under simulated sunlight. Obviously, CNH showed the highest removal rate. About 92% of UO_2^{2+} was reduced in 30 min and reached reaction equilibrium in 60 min, and U(VI) of 50 ppm could be almost completely removed (Fig. 6(a)). In contrast, the CNNH with the destroyed conjugated structure almost lost its reduction efficiency, which was only 3.2%. Then, the removal effect of U(VI) by CNH in a wide range of pH was explored (Fig. 6(b)), and we found that it lost its reducibility in solid acid environment, which was consistent with most of the literature reports [66–68], it could be attributed to the competition between H^+ protons and delocalized π * electrons in a solid acid environment, resulting in a decrease in the efficiency of reducing U(VI). The reduction efficiency of U(VI) by each catalyst was tested in the environment of simulated nuclear wastewater, and the pH was adjusted to the optimum value (Fig. 6(c)).

Similarly, CNH showed the best reduction efficiency, and 99.6% U (VI) could be removed within 60 min. Similarly, CNNH offers little reduction efficiency, which further explains that the integrity of the conjugated system determines that the π * electrons undergo a delocalization transition to participate in the reduction reaction. Fig. 6(d) shows the reduction efficiency of CNH in the presence of various interfering ions. It can be found that the reduction rate of CNH is not significantly affected, and the removal rate is more than 90%. Combined with cycle experiments, it can be concluded that CNH has high stability and excellent performance for U(VI) removal in the simulated nuclear wastewater environment.

As shown in Fig. 6(f), the XPS spectrum of U 4 f before and after photocatalysis was measured. The adsorption of U(VI) on the catalyst under dark conditions is all hexavalent uranium [69–71]. After the photocatalysis process, the species peak of U(IV) appears on the surface of CNH, indicating that CNH can effectively reduce U(VI) to U(IV) and realize the possibility of photocatalytic reduction/recovery of uranium. Under light conditions, the ESR signals of DMPO-·O_2^- (anhydrous methanol as solvent) and DMPO-·OH (in water) appear to be significantly enhanced (Fig. 6(g)), it means that the CNH photocatalyst retains strong redox performance due to the influence of the built-in electric field, and its efficient electrons-holes pairs separation efficiency allows the photogenerated carriers to generate·O_2^- and·OH radicals during the reaction process. The side reflects the high charge separation efficiency and carrier density in CNH [69].

In addition, we supplemented the effect of solution salinity on the reduction efficiency of the catalyst, and also explored the addition of different catalysts, different types of sacrificial agents and different amounts of anhydrous methanol effect on reduction efficiency under simulated nuclear wastewater, as shown in Fig. S4. The amount of

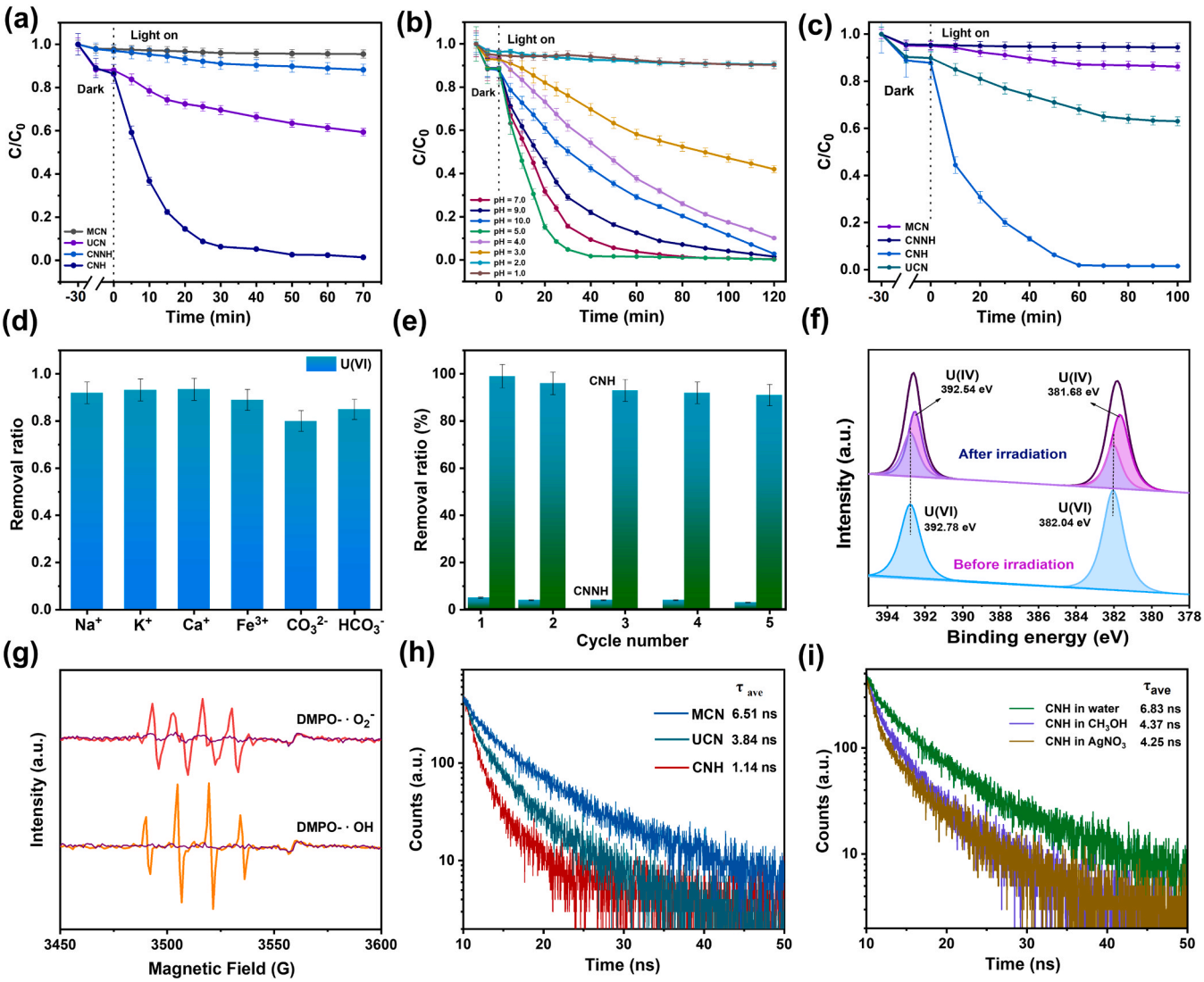

Fig. 6. Photoreaction kinetics of the catalyst in (a) pure water system, (b) a wide range of pH, and (c) simulated nuclear wastewater; (d) Effect of various interfering ions on the CNH. (e) Cycling experiments of CNH; (f) U 4 f spectra of CNH before and after reaction; (g) ESR signals of DMPO-·OH and DMPO-·O_2^-; (h) Time-resolved PL decay curves of MCN, UCN, and CNH; (i) Time-resolved PL decay curves of CNH in water, anhydrous methanol (CH_3OH), and Ag^+.

catalyst has a direct impact on the economic efficiency of photocatalytic reduction of uranium. Experiments have shown that a low dosage of 0.1 g/L can achieve a reduction efficiency of 99.6%. The high salinity of radioactive wastewater is also one of the main challenges for reducing U (VI). Therefore, we additionally added 10 mmol/L NaCl, 10 mmol/L $NaNO_3$ and 5 mmol/L Na_2SO_4 to the uranyl solution to evaluate the effect of salinity on the reduction efficiency of U(VI). The results showed that the reduction efficiency of uranium was only slightly affected by these additives, demonstrating the high resistance of the catalyst to high salinity. In order to confirm the stability of the material, as shown in Fig. 6(e), the catalyst can still maintain a good reduction efficiency after five elution cycle. In addition, we soaked the uranium-loaded material after photocatalytic reduction in the acidic uranium-containing simulated nuclear wastewater solution for 7 days. SEM and XRD showed that the structure of the material did not change (Fig. S5), which indicated that the material could remain stable for a long time in the nuclear wastewater environment properties, suggesting that the material may be suitable for use in nuclear emergencies.

To further proof the main reactive radicals that play a role in the U (VI) photoreduction process, we used p-benzoquinone (P-BQ), isopropanol (IPA) and sodium persulfate ($Na_2S_2O_8$) as scavenger for·O_2^-,·OH and e^-. As shown in Fig. S9, the addition of IPA did not affect the reduction of U(VI), the reduction efficiency decreased after the addition of P-BQ, and almost lost the reduction efficiency after the addition of $Na_2S_2O_8$, combined with ESR spectra, we can conclude that photogenerated electrons participate in the photoreduction reaction process of U(VI) as the central power species. In addition, the time resolved photoluminescence (PL) decay curves of MCN, UCN, and CNH were tested, as well as their respective decay curves in water, anhydrous methanol, and $AgNO_3$ solutions. Fig. 6(h) shows that CNH exhibits the fastest attenuation dynamics. Average radiation lifetime of MCN, UCN, and CNH (τA) is 6.51, 3.84, and 1.14 ns, respectively. The accelerated photoluminescence (PL) decay indicates that the CNH homojunction effectively promotes exciton dissociation and significantly improves the effective charge transfer. In addition, Fig. 6(i) shows that CNH exhibits faster fluorescence attenuation in anhydrous methanol and $AgNO_3$ solution environments, indicating the effective elimination of high-energy holes and electrons in homogeneous junctions [72,73]. Therefore, the effective separation of electrons and holes can be achieved based on the strong built-in electric field.

Fig. 7 simply shows the reaction mechanism for reducing U (VI) with CNH. CNH structure is a π-conjugated molecule composed of a triazine structure and double bond. It can also be regarded as a conjugated system formed by strong π-π stacking of Re-CN and Ox-CN in the molecule. Under the irradiation of simulated sunlight with sufficient energy, the π * electrons in the conduction bands of Re-CN and Ox-CN are excited to become photogenerated electrons and exhibit π→π * and n→π * electron transitions in the CNH conjugated system. This can be proved by the characteristic peaks in the UV–vis spectrum [47,48,74]. At this time, the electrons with delocalized transition can directly participate in the reduction reaction of uranyl ions. At the same time, the difference in energy band structure leads to the recombination of the electrons in the Ox-CN conduction band and the holes in the Re-CN valence band to a certain extent, thus forming a strong built-in electric field in the π-conjugated molecules. Under the action of the built-in electric field force, the photogenerated carriers are further separated, resulting in the local aggregation of electrons in Re-CN, which significantly improves the efficiency of photocatalytic reduction of U(VI). In summary, the delocalization of π * electrons in π-conjugated molecules and the strong built-in electric field in molecules promote the separation and aggregation of photogenerated electrons. The photocatalytic process we mentioned provides a possibility mechanism for the effective photoreduction of U (VI).

4. Conclusion

The conjugated molecule CNH was successfully constructed through strong π-π stacking of Re-CN and Ox-CN, forming an intramolecular donor-acceptor (D-A) structure due to the π-π interaction. A strong built-in electric field forms for CNH, leading to the local separation and aggregation of photogenerated carriers upon irradiation with sufficient energy. Electrons and holes accumulate in the conduction band and valence band of Re-CN and Ox-CN, respectively. Under simulated sunlight, the CNH photocatalyst achieved 99.6% efficiency in reducing U (VI) within 60 min. This excellent activity originates from CNH's effective carrier transfer channels (conjugated molecule π→π * and n→π * electron transitions) contributing to spatially separated carrier-rich regions.

In summary, the built-in electric field inherent in CNH's unique structure enhances the separation efficiency of photogenerated carriers and promotes the regional aggregation of photogenerated electrons and holes. The distinctive π-electron delocalization and transition improve carrier density and further boost the photocatalytic reduction efficiency of uranium (VI). This work combines π-conjugated molecules and homojunctions to realize the built-in electric field in CNH molecules, adjusting the molecular energy band structure and achieving excellent

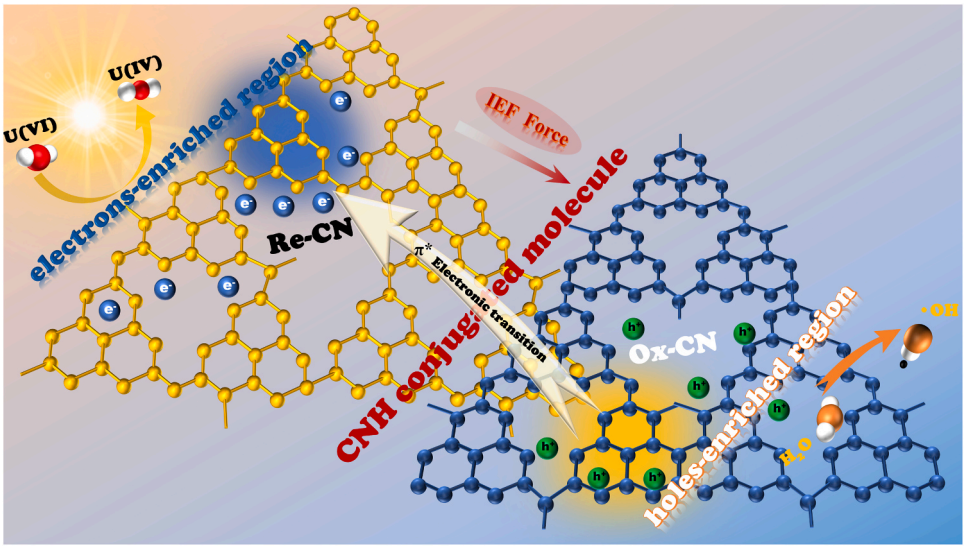

Fig. 7. Schematic diagram of U(VI) photoreduction reaction process.

charge separation and transfer. Consequently, our research offers a new direction for efficiently removing uranium pollution in the future and highlights the potential of π-electron delocalization of conjugated molecules to enhance photocatalytic applications.

CRediT authorship contribution statement

Zhangmeng Liu: Conceptualization, Methodology, Data curation, Writing – original draft. **Shuaiqi Yao**: Visualization, Investigation. **Anrang Zhang:** Validation. **Yayao Li**: Visualization, Investigation. **Yunzhi Fu:** Supervision. **Qixin Zhou:** Writing – review & editing.

Declaration of Competing Interest

The authors declare that they have no known competing financial interests or personal relationships that could have appeared to influence the work reported in this paper.

Data availability

Data will be made available on request.

Acknowledgements

This work was financially supported by the National Natural Science Foundation of China (No. 22162009)

Appendix A. Supporting information

Supplementary data associated with this article can be found in the online version at doi:10.1016/j.apcatb.2023.123023.

References

[1] Y. Cai, Y. Zhang, Z. Lv, S. Zhang, F. Gao, M. Fang, M. Kong, P. Liu, X. Tan, B. Hu, X. Wang, Highly efficient uranium extraction by a piezo catalytic reduction-oxidation process, Appl. Catal. B: Environ. 310 (2022), 121343.
[2] M. Chen, T. Liu, X. Zhang, R. Zhang, S. Tang, Y. Yuan, Z. Xie, Y. Liu, H. Wang, K. V. Fedorovich, N. Wang, Photoinduced enhancement of uranium extraction from seawater by MOF/Black Phosphorus quantum dots heterojunction anchored on cellulose nanofiber aerogel, Adv. Funct. Mater. 31 (2021) 2100106.
[3] K. Yu, L. Tang, X. Cao, Z. Guo, Y. Zhang, N. Li, C. Dong, X. Gong, T. Chen, R. He, W. Zhu, Semiconducting metal–organic frameworks decorated with spatially separated dual cocatalysts for Efficient Uranium(VI) Photoreduction, Adv. Funct. Mater. 32 (2022) 2200315.
[4] Y. Jiang, H.Y. Chen, J.Y. Li, J.F. Liao, H.H. Zhang, X.D. Wang, D.B. Kuang, Z-scheme 2D/2D heterojunction of $CsPbBr_3/Bi_2WO_6$ for improved photocatalytic CO_2 reduction, Adv. Funct. Mater. 30 (2020) 2004293.
[5] B. Lei, W. Cui, P. Chen, L. Chen, J. Li, F. Dong, C–doping induced oxygen-vacancy in WO_3 nanosheets for CO_2 activation and photoreduction, ACS Catal. 12 (2022) 9670–9678.
[6] Z. Li, C. Mao, Q. Pei, P.N. Duchesne, T. He, M. Xia, J. Wang, L. Wang, R. Song, A. A. Jelle, Engineered disorder in CO_2 photocatalysis, Nat. Commun. 13 (2022) 7205.
[7] K. Feng, R. Song, J. Xu, Y. Chen, C. Lu, Y. Li, W. Hofer, H. Lin, Z. Kang, J. Zhong, The S-Fe (Ni) Sub-Surface active sites for efficient and stable overall water splitting, Appl. Catal. B: Environ. (2023), 122365.
[8] G. Wan, L. Yin, X. Chen, X. Xu, J. Huang, C. Zhen, H. Zhu, B. Huang, W. Hu, Z. Ren, Photocatalytic overall water splitting over $PbTiO_3$ modulated by oxygen vacancy and ferroelectric polarization, J. Am. Chem. Soc. 144 (2022) 20342–20350.
[9] F. Raziq, A. Aligayev, H. Shen, S. Ali, R. Shah, S. Ali, S.H. Bakhtiar, A. Ali, N. Zarshad, A. Zada, Exceptional photocatalytic activities of rGO modified (B, N) Co-Doped WO_3, coupled with CdSe QDs for one photon Z-scheme system: A joint experimental and DFT study, Adv. Sci. 9 (2022) 2102530.
[10] P. Li, J. Wang, Y. Wang, L. Dong, W. Wang, R. Geng, Z. Ding, D. Luo, D. Pan, J. Liang, Ultrafast recovery of aqueous uranium: Photocatalytic U(VI) reduction over $CdS/g\text{-}C_3N_4$, Chem. Eng. J. 425 (2021), 131552.
[11] M.-Y. Liu, Y.-W. Wei, C.-C. Wang, P. Wang, Adsorption and photocatalytic desorption toward Cr (VI) over defect-induced hierarchically porous UiO-66-$(OH)_2$: A sustainable approach, Environ. Sci.: Nano (2023).
[12] X.-H. Yi, Y. Gao, C.-C. Wang, Y.-H. Li, H.-Y. Chu, P. Wang, Photocatalytic Cr (VI) reduction over MIL-88A (Fe) on polyurethane sponge: From batch to continuous-flow operation, Chin. Chem. Lett. (2022), 108029.
[13] W. Tian, J. Han, L. Wan, N. Li, D. Chen, Q. Xu, H. Li, J. Lu, Enhanced piezocatalytic activity in ion-doped SnS_2 via lattice distortion engineering for BPA degradation and hydrogen production, Nano Energy (2023), 108165.
[14] C. Zhao, L. Meng, H. Chu, J.-F. Wang, T. Wang, Y. Ma, C.-C. Wang, Ultrafast degradation of emerging organic pollutants via activation of peroxymonosulfate over Fe_3C/Fe@ NCx: Singlet oxygen evolution and electron-transfer mechanisms, Appl. Catal. B: Environ. 321 (2023), 122034.
[15] Q. Su, J. Li, B. Wang, Y. Li, Direct Z-scheme Bi_2MoO_6/UiO-66-NH_2 heterojunctions for enhanced photocatalytic degradation of ofloxacin and ciprofloxacin under visible light, Appl. Catal. B: Environ. 318 (2022), 121820.
[16] Z. Zhang, R. Ji, Q. Sun, J. He, D. Chen, N. Li, H. Li, A. Marcomini, Q. Xu, J. Lu, Enhanced photocatalytic degradation of 2-chlorophenol over Z-scheme heterojunction of CdS-decorated oxygen-doped $g\text{-}C_3N_4$ under visible-light, Appl. Catal. B: Environ. 324 (2023), 122276.
[17] Z. Dai, J. Lian, Y. Sun, L. Li, H. Zhang, N. Hu, D. Ding, Fabrication of $g\text{-}C_3N_4/Sn_3O_4$/Ni electrode for highly efficient photoelectrocatalytic reduction of U(VI), Chem. Eng. J. 433 (2022), 133766.
[18] X. Ding, K. Zhao, L. Zhang, Enhanced photocatalytic removal of sodium pentachlorophenate with self-doped Bi_2WO_6 under visible light by generating more superoxide ions, Environ. Sci. Technol. 48 (2014) 5823–5831.
[19] W. Dong, H. Gao, l Siya, Z. Dong, Z. Zheng, Y. Wu, X. Zhu, Z. Cheng, Y. Liu, Y. Wang, C. Xiaohong, Y. Wang, Z. Zhang, Y. Liu, Photocatalytic applications of heterostructure Ag_2S/TiO_2 nanotube arrays for U(VI) reduction and phenol degradation, J. Solid State Chem. 310 (2022), 123010.
[20] Z. Dong, Z. Zhang, Z. Li, Y. Wang, F. Yu, Z. Cheng, Y. Dai, X. Cao, Y. Wang, Y. Liu, X. Fan, Double-shelled hollow nanosphere assembled by TiO_2@surface sulfate functionalized CdS for boosting photocatalysis reduction of U(VI) under seawater conditions, Chem. Eng. J. 431 (2022), 133256.
[21] Z. Li, Z. Zhang, Z. Dong, F. Yu, M. Ma, Y. Wang, Y. Wang, Y. Liu, J. Liu, X. Cao, Y. Liu, Solar light-responsive CdS/UiO-66-NH_2 for ultrafast uranium reduction from uranium-containing mine wastewater without external sacrificial agents, Sep. Purif. Technol. 283 (2022), 120195.
[22] B. Chen, G. Zhang, L. Chen, J. Kang, Y. Wang, S. Chen, Y. Jin, H. Yan, C. Xia, Visible light driven photocatalytic removal of uranium(VI) in strongly acidic solution, J. Hazard. Mater. 426 (2022), 127851.
[23] J. Chen, H. Wu, G. Sheng, H. Li, M. Li, X. Guo, H. Dong, Graphene oxide-mediated the reduction of U(VI), Re(VII), Se(VI) and Se(IV) by Fe(II) in aqueous solutions investigated via combined batch, DFT calculation and spectroscopic approaches, Chem. Eng. J. 433 (2022), 133844.
[24] L. Chen, M. Wakeel, T.U. Haq, C. Chen, X. Ren, Insight into UV-induced simultaneous photocatalytic degradation of $Ti_3C_2T_x$ MXene and reduction of U(VI), J. Hazard. Mater. 430 (2022), 128377.
[25] T. Chen, T. Liu, L. Zhou, M. Li, Q. Meng, K. Yu, J. Lian, W. Zhu, Ternary boron carbon nitrides hollow nanotubes with tunable p-n homojunction for photo-assisted uranium extraction: A combined batch, EXAFS and DFT calculations, Appl. Catal. B: Environ. 318 (2022), 121815.
[26] Z. Dong, Z. Zhang, T. Wang, D. Zeng, Z. Cheng, Y. Wang, X. Cao, Y. Wang, Y. Liu, X. Fan, Ingenious design of ternary hollow nanosphere with shell hierarchical tandem heterojunctions toward optimized Visible-light photocatalytic reduction of U(VI), Sep. Purif. Technol. 286 (2022), 120418.
[27] X. Zhong, Q. Ling, Z. Ren, B. Hu, Immobilization of U(VI) onto covalent organic frameworks with the different periodic structure by photocatalytic reduction, Appl. Catal. B: Environ. 326 (2023), 122398.
[28] Y. Yang, X. Chu, H.Y. Zhang, R. Zhang, Y.H. Liu, F.M. Zhang, M. Lu, Z.D. Yang, Y. Q. Lan, Engineering beta-ketoamine covalent organic frameworks for photocatalytic overall water splitting, Nat. Commun. 14 (2023) 593.
[29] D. Chen, W. Chen, Y. Wu, L. Wang, X. Wu, H. Xu, L. Chen, Covalent organic frameworks containing dual O_2 reduction centers for overall photosynthetic hydrogen peroxide production, Angew. Chem. Int. Ed. 9 (2023), e202217479.
[30] S.L. Yang, H.W. Lv, H. Zhong, D.Q. Yuan, X.C. Wang, R.H. Wang, Transformation of covalent organic frameworks from N-Acylhydrazone to oxadiazole linkages for smooth electron transfer in photocatalysis, Angew. Chem. Int. Ed. 61 (2022), e202115655.
[31] W. Helweh, N.C. Flanders, S. Wang, B.T. Phelan, P. Kim, M.J. Strauss, R.L. Li, M. S. Kelley, M.S. Kirschner, D.O. Edwards, Layered structures of assembled imine-linked macrocycles and two-dimensional covalent organic frameworks give rise to prolonged exciton lifetimes, J. Mater. Chem. C. 10 (2022) 3015–3026.
[32] S.-Y. Hu, Y.-N. Sun, Z.-W. Feng, F.-O. Wang, Y.-k Lv, Design and construction strategies to improve covalent organic frameworks photocatalyst's performance for degradation of organic pollutants, Chemosphere 286 (2022), 131646.
[33] X. Ren, G. Liao, Z. Li, H. Qiao, Y. Zhang, X. Yu, B. Wang, H. Tan, L. Shi, X. Qi, Two-dimensional MOF and COF nanosheets for next-generation optoelectronic applications, Coord. Chem. Rev. 435 (2021), 213781.
[34] X. Zhao, P. Pachfule, A. Thomas, Covalent organic frameworks (COFs) for electrochemical applications, Chem. Soc. Rev. 50 (2021) 6871–6913.
[35] W.R. Cui, C.R. Zhang, R.H. Xu, X.R. Chen, W. Jiang, Y.J. Li, R.P. Liang, L. Zhang, J.-D. Qiu, Rational design of covalent organic frameworks as a groundbreaking uranium capture platform through three synergistic mechanisms, Appl. Catal. B: Environ. 294 (2021), 120250.
[36] Y. Zhi, Z. Li, X. Feng, H. Xia, Y. Zhang, Z. Shi, Y. Mu, X. Liu, Covalent organic frameworks as metal-free heterogeneous photocatalysts for organic transformations, J. Mater. Chem. A 5 (2017) 22933–22938.
[37] M.Y. Gao, C.C. Li, H.L. Tang, X.J. Sun, H. Dong, F.M. Zhang, Boosting visible-light-driven hydrogen evolution of covalent organic frameworks through compositing with MoS_2: a promising candidate for noble-metal-free photocatalysts, J. Mater. Chem. A 7 (2019) 20193–20200.
[38] X.Y. Zhang, J.J. Wang, P. Li, Z.Y. Tan, J.H. Zeng, Y.R. He, N. Habibul, Removal of U (VI) from aqueous solution via photocatalytic reduction over $WO_3/g\text{-}C_3N_4$ composite under visible light, Chem. Eng. J. 428 (2022), 131209.

[39] H. Wang, H. Guo, N. Zhang, Z. Chen, B. Hu, X. Wang, Enhanced photoreduction of U(VI) on C_3N_4 by Cr(VI) and Bisphenol A: ESR, XPS, and EXAFS investigation, Environ. Sci. Technol. 53 (2019) 6454–6461.

[40] Y. Liu, S. Wu, J. Liu, S. Xie, Y. Liu, Synthesis of g-C_3N_4/TiO_2 nanostructures for enhanced photocatalytic reduction of U(VI) in water, RSC Adv. 11 (2021) 4810–4817.

[41] J. Wu, X. Xi, W. Zhu, Z. Yang, P. An, Y. Wang, Y. Li, Y. Zhu, W. Yao, G. Jiang, Boosting photocatalytic hydrogen evolution via regulating Pt chemical states, Chem. Eng. J. 442 (2022), 136334.

[42] W. Li, Z. Wei, K. Zhu, W. Wei, J. Yang, J. Jing, D.L. Phillips, Y. Zhu, Nitrogen-defect induced trap states steering electron-hole migration in graphite carbon nitride, Appl. Catal. B: Environ. 306 (2022), 121142.

[43] F.K. Kessler, Y. Zheng, D. Schwarz, C. Merschjann, W. Schnick, X. Wang, M. J. Bojdys, Functional carbon nitride materials—design strategies for electrochemical devices, Nat. Rev. Mater. 2 (2017) 1–17.

[44] H. Liu, H. Li, J. Lu, S. Zeng, M. Wang, N. Luo, S. Xu, F. Wang, Photocatalytic cleavage of C–C bond in lignin models under visible light on mesoporous graphitic carbon nitride through π–π stacking interaction, ACS Catal. 8 (2018) 4761–4771.

[45] X. Wang, S. Blechert, M. Antonietti, Polymeric graphitic carbon nitride for heterogeneous photocatalysis, ACS Catal. 2 (2012) 1596–1606.

[46] Z. Teng, Q. Zhang, H. Yang, K. Kato, W. Yang, Y.-R. Lu, S. Liu, C. Wang, A. Yamakata, C. Su, Atomically dispersed antimony on carbon nitride for the artificial photosynthesis of hydrogen peroxide, Nat. Catal. 4 (2021) 374–384.

[47] G. Zhao, B. Li, X. Yang, X. Zhang, Z. Li, D. Jiang, H. Du, C. Zhu, H. Li, C. Xue, Y. Yuan, Two birds with one stone: Engineering polymeric carbon nitride with n-π* electronic transition for extending light absorption and reducing charge recombination, Adv. Powder Mater. 2 (2023), 100077.

[48] F.-Y. Su, C.-Q. Xu, Y.-X. Yu, W.-D. Zhang, Carbon self-doping induced activation of n-π* electronic transitions of g-C_3N_4 nanosheets for efficient photocatalytic H_2 evolution, ChemCatChem 8 (2016) 3527–3535.

[49] W. Shang, W. Liu, X. Cai, J. Hu, J. Guo, C. Xin, Y. Li, N. Zhang, N. Wang, C. Hao, Y. Shi, Insights into atomically dispersed reactive centers on g-C_3N_4 photocatalysts for water splitting, Adv. Powder Mater. 2 (2023), 100094.

[50] Q. Zhou, Y. Guo, Z. Ye, Y. Fu, Y. Guo, Y. Zhu, Carbon nitride photocatalyst with internal electric field induced photogenerated carriers spatial enrichment for enhanced photocatalytic water splitting, Mater. Today 58 (2022) 100–109.

[51] W.-J. Ong, L.-L. Tan, Y.H. Ng, S.-T. Yong, S.-P. Chai, Graphitic carbon nitride (g-C_3N_4)-based photocatalysts for artificial photosynthesis and environmental remediation: are we a step closer to achieving sustainability? Chem. Rev. 116 (2016) 7159–7329.

[52] L. Gross, F. Mohn, P. Liljeroth, J. Repp, F.J. Giessibl, G. Meyer, Measuring the charge state of an adatom with noncontact atomic force microscopy, Science 324 (2009) 1428–1431.

[53] Y. Guo, W. Shi, Y. Zhu, Internal electric field engineering for steering photogenerated charge separation and enhancing photoactivity, EcoMat 1 (2019).

[54] J. Zhu, F. Fan, R. Chen, H. An, Z. Feng, C. Li, Direct imaging of highly anisotropic photogenerated charge separations on different facets of a single $BiVO_4$ photocatalyst, Angew. Chem. 127 (2015) 9239–9242.

[55] Z. Zhang, J.T. Yates Jr, Band bending in semiconductors: chemical and physical consequences at surfaces and interfaces, Chem. Rev. 112 (2012) 5520–5551.

[56] X. Zhong, Q. Ling, S. Wang, B. Hu, Visible-light-driven 2D/2D Bismuth oxyhalides/covalent organic framework heterojunctions for synchronous photocatalytic U(VI) reduction and bisphenol A degradation, J. Environ. Chem. Eng. 10 (2022), 108097.

[57] T. Kanata-Kito, M. Matsunaga, H. Takakura, Y. Hamakawa, T. Nishino, Photoreflectance characterization of built-in potential in MBE-produced As-grown GaAs surface, Modul. Spectrosc., SPIE (1990) 56–65.

[58] J. Jing, J. Yang, W. Li, Z. Wu, Y. Zhu, Construction of interfacial electric field via Dual-Porphyrin heterostructure boosting photocatalytic hydrogen evolution, Adv. Mater. 34 (2022) 2106807.

[59] J.S. Im, H. Kollmer, J. Off, A. Sohmer, F. Scholz, A. Hangleiter, Reduction of oscillator strength due to piezoelectric fields in GaN/$Al_xGa_{1-x}N$ quantum wells, Phys. Rev. B 57 (1998) R9435.

[60] E. Thimsen, F. Le Formal, M. Gratzel, S.C. Warren, Influence of plasmonic Au nanoparticles on the photoactivity of Fe_2O_3 electrodes for water splitting, Nano Lett. 11 (2011) 35–43.

[61] K. Sivula, F.L. Formal, M. Gratzel, WO_3−Fe_2O_3 photoanodes for water splitting: A host scaffold, guest absorber approach, Chem. Mater. 21 (2009) 2862–2867.

[62] F. Le Formal, K. Sivula, M. Grätzel, The transient photocurrent and photovoltage behavior of a hematite photoanode under working conditions and the influence of surface treatments, J. Phys. Chem. C. 116 (2012) 26707–26720.

[63] X. Chen, J. Wang, Y. Chai, Z. Zhang, Y. Zhu, Efficient photocatalytic overall water splitting induced by the giant internal electric field of Ag-C_3N_4/rGO/PDIP Z-scheme heterojunction, Adv. Mater. 33 (2021) 2007479.

[64] B. Li, S. Liu, C. Lai, G. Zeng, M. Zhang, M. Zhou, D. Huang, L. Qin, X. Liu, Z. Li, Unravelling the interfacial charge migration pathway at atomic level in 2D/2D interfacial Schottky heterojunction for visible-light-driven molecular oxygen activation, Appl. Catal. B: Environ. 266 (2020), 118650.

[65] G. Liu, J. Shi, F. Zhang, Z. Chen, J. Han, C. Ding, S. Chen, Z. Wang, H. Han, C. Li, A tantalum nitride photoanode modified with a hole-storage layer for highly stable solar water splitting, Angew. Chem. Int Ed. Engl. 53 (2014) 7295–7299.

[66] X. Liu, X. Wang, W. Jiang, C.-R. Zhang, L. Zhang, R.-P. Liang, J.-D. Qiu, Covalent organic framework modified carbon nanotubes for removal of uranium (VI) from mining wastewater, Chem. Eng. J. 450 (2022), 138062.

[67] Y. Li, L. Shi, Y. Mao, Y. Zhang, H. Wang, Efficient reduction of uranyl under aerobic conditions by sodium and potassium co-doped carbon nitride, Chem. Eng. J. 446 (2022), 136872.

[68] H. Wan, Y. Li, M. Wang, Q. Zhao, Y. Fu, Y. Chen, P. He, L. Wu, Q. Meng, T. Ma, J. Yang, T. Duan, Boosting efficient U(VI) immobilization via synergistic Schottky heterojunction and hierarchical atomic-level injected engineering, Chem. Eng. J. 430 (2022), 133139.

[69] F. Yu, Z. Zhu, S. Wang, J. Wang, Z. Xu, F. Song, Z. Dong, Z. Zhang, Novel donor-acceptor-acceptor ternary conjugated microporous polymers with boosting forward charge separation and suppressing backward charge recombination for photocatalytic reduction of uranium (VI), Appl. Catal. B: Environ. 301 (2022), 120819.

[70] F. Yu, Z. Zhu, C. Li, W. Li, R. Liang, S. Yu, Z. Xu, F. Song, Q. Ren, Z. Zhang, A redox-active perylene-anthraquinone donor-acceptor conjugated microporous polymer with an unusual electron delocalization channel for photocatalytic reduction of uranium (VI) in strongly acidic solution, Appl. Catal. B: Environ. 314 (2022), 121467.

[71] H. Yang, X. Liu, M. Hao, Y. Xie, X. Wang, H. Tian, G.I.N. Waterhouse, P.E. Kruger, S.G. Telfer, S. Ma, Functionalized Iron-Nitrogen-Carbon electrocatalyst provides a reversible electron transfer platform for efficient uranium extraction from seawater, Adv. Mater. 33 (2021) 2106621.

[72] X. She, J. Wu, H. Xu, J. Zhong, Y. Wang, Y. Song, K. Nie, Y. Liu, Y. Yang, M.T. F. Rodrigues, High efficiency photocatalytic water splitting using 2D α-Fe_2O_3/g-C_3N_4 Z-scheme catalysts, Adv. Energy Mater. 7 (2017) 1700025.

[73] X. Chen, F. Liu, X. Yan, Y. Yang, Q. Chen, J. Wan, L. Tian, Q. Xia, X. Chen, $Ag_2Mo_3O_{10}$ nanorods decorated with Ag_2S nanoparticles: visible-light photocatalytic activity, photostability, and charge transfer, Chem. Eur. J. 21 (2015) 18711–18716.

[74] J. Shao, H. Fei, H. Li, L. Yang, M. Li, J. Gao, H. Liao, J. Lu, Synergizing n → π* electronic transition and plasmonic hot electron injection enhances carrier generation of S-doped carbon nitride decorated with Au nanoparticles for Cr(VI) degradation, Sep. Purif. Technol. 297 (2022), 121515.